



Supplement of

The sensitivity of primary productivity in Disko Bay, a coastal Arctic ecosystem, to changes in freshwater discharge and sea ice cover

Eva Friis Møller et al.

Correspondence to: Eva Friis Møller (efm@ecos.au.dk)

The copyright of individual parts of the supplement might differ from the article licence.

Abstract. The Greenland Ice Sheet is melting, and the rate of ice loss has increased 6-fold since the 1980s. At the same time, the Arctic sea ice extent is decreasing. Melt water runoff and sea ice reduction both influence light and nutrient availability in the coastal ocean with implications for the timing, distribution and magnitude of phytoplankton production. However, the integrated effect of both glacial and sea ice melt is highly variable in time and space, making it challenging to quantify. In this study, we evaluate the relative importance of these processes for the primary productivity of Disko Bay, West Greenland, one of the most important areas for biodiversity and fisheries around Greenland. We use a high-resolution 3D coupled hydrodynamic-biogeochemical model for 2004 to 2018 validated against *in situ* observations and remote sensing products. The model estimated net primary production (NPP) varied between 90-147 gC m⁻² year⁻¹ during 2004-2018, a period with variable freshwater discharges and sea ice cover. NPP correlated negatively with sea ice cover, and positively with freshwater discharge. Freshwater discharge had a strong local effect within ~25 km of the source sustaining productive hot spot's during summer. When considering the annual NPP at bay scale, sea ice cover was the most important controlling factor. In scenarios with no sea ice in spring, the model predicted ~30% increase in annual production compared to a situation with high sea ice cover. Our study indicates that decreasing ice cover and more freshwater discharge can work synergistically and will likely increase primary productivity of the coastal ocean around Greenland.

36 1 Supplements

37 1.1 Supplement, Table

38 Table A.1. Constants in the FlexSem ecological Disko Bay model.

Parameter	Description	Numerical value	Units
Phytoplankton			
α_1	Half-saturation uptake diatoms	0.55	mmol-N m ⁻³
α_2	Half-saturation uptake flagellates	0.45	mmol-N m ⁻³
RD_0	Maximum uptake diatoms at 0°C	1.50	d ⁻¹
RF_0	Maximum uptake flagellates at 0°C	0.75	d ⁻¹
S_{DIA}	Sinking rate diatoms	-1	m d ⁻¹
$Iopt_{dia}$	Optimum PAR diatoms	95	W m ⁻²
$Iopt_{flag}$	Optimum PAR flagellates	105	W m ⁻²
k_c	Attenuation constant self-shading	0.03	m ² (mg Chl a) ⁻¹
LPN	Loss rate phytoplankton to nutrients at 0°C	0.03	d ⁻¹
LPD	Loss rate phytoplankton to detritus at 0°C	0.02	d ⁻¹
Ths_1	Half-saturation temperature diatoms	12	°C
Ths_2	Half-saturation temperature flagellates	7	°C
Q_{10}	Maintenance temperature coefficient	0.07	°C ⁻¹
RFR	Redfield ratio N:P (mol-based)	16:1	fraction
N:Si	Si:N-ratio (mol-based)	1.1	fraction
Zooplankton			
$Imax_{MEZ}$	Maximum grazing mesozooplankton at 12°C	0.47	d ⁻¹
$Imax_{MIZ}$	Maximum grazing microzooplankton at 0°C	0.60	d ⁻¹
K_{MEZ}	Half-saturation ingestion mesozooplankton	0.32	mmol-N m ⁻³
K_{MIZ}	Half-saturation ingestion microzooplankton	0.60	mmol-N m ⁻³
AE_{MEZ}	Assimilation efficiency mesozooplankton	0.65	fraction
AE_{MIZ}	Assimilation efficiency microzooplankton	0.60	fraction
R_{MEZ}	Active respiration mesozooplankton	0.29	fraction
R_{MIZ}	Active respiration microzooplankton	0.35	fraction
β_{MEZ}	Basal respiration mesozooplankton at 0°C	0.005	d ⁻¹
β_{MIZ}	Basal respiration microzooplankton at 0°C	0.03	d ⁻¹
$pref_{DI}$	Grazing preference for diatoms by MEZ and MIZ	1.0	fraction
$pref_{FL}$	Grazing preference for flagellates by MEZ and MIZ	1.0	fraction
$pref_{MIZ}$	Grazing preference for microzooplankton by MEZ	1.0	fraction
$Mmax_{MEZ}$	Maximum mortality mesozooplankton at 0°C	0.004	d ⁻¹
$Mmax_{MIZ}$	Maximum mortality microzooplankton at 0°C	0.030	d ⁻¹
KM_{MEZ}	Half-saturation mortality mesozooplankton	0.07	mmol-N m ⁻³
KM_{MIZ}	Half-saturation mortality microzooplankton	0.02	mmol-N m ⁻³
Ths_{MIZ}	Half-saturation temperature microzooplankton	4	°C
SVM_{MEZ}	Seasonal vertical migration mesozooplankton	0-25	m d ⁻¹
Detritus and nutrients			
DN	Mineralisation of detritus at 0°C	0.001	d ⁻¹
DN_{Si}	Mineralisation of Si-detritus at 0°C	0.0001	d ⁻¹

NI_0	Maximum nitrification rate at 0 °C	0.02	d^{-1}
K_{nit}	Oxygen half-saturation in nitrification	3.75	$mmol-O_2\ m^{-3}$
K_{denit}	Nitrate half-saturation in denitrification	0.135	$mmol-NO_3\ m^{-3}$
T_{sen}	Temperature coefficient on recycling processes	0.07	$^{\circ}C^{-1}$
$SEDR$	Sinking rate detritus	-20	$m\ d^{-1}$
RQN	Respiratory quotient in nitrification	2.0	$O_2:NO_3$
RQC	Respiratory quotient in detritus	1.0	$O_2:Organic-N$
S_{DET}	Settling rate detritus	20	$m\ d^{-1}$

39

40

1.2 Supplement, the ocean model (HYCOM)

The ocean model (HYCOM) has 40 hybrid vertical levels, combining isopycnals with z-level coordinates and sigma coordinates. Tides are included internally within the ocean model using eight constituents and similar tides are added at the open boundaries using the Oregon State University TOPEX/Poseidon Global Inverse Solution (TPXO 8.2,) Egbert and Erofeeva, 2002). More than 100 rivers are included as monthly climatological discharges obtained from the Global Runoff Data Centre (GRDC, <http://grdc.bafg.de>) and scaled as prescribed by Dai and Trenberth (2002)(Dai and Trenberth, 2002). In addition the globally gridded Core v2 runoff data (Large and Yeager, 2009) is added for Greenland, the Canadian Archipelago, Svalbard, and islands within the Arctic Ocean.

The sea ice model (CICE) describes the dynamics and thermodynamics of the sea ice as described by Rasmussen et al, 2018 (Rasmussen et al., 2018). The dynamics is driven by drag from wind and ocean, surface tilt of the ocean, Coriolis force, and the internal strength of sea ice that will resist movement of the ice pack. The internal strength is based on the Elastic-Viscous-Plastic (EVP) sea-ice rheology (Hunke, 2001), that originates from the Viscous-Plastic (VP) described by Hibler (1979)(Hibler, 1979). CICE includes 5 thickness categories of sea ice within each grid cell in order to describe the inhomogeneity. The thermodynamics prescribes a vertical temperature profile with a resolution of four sea ice layers and one layer of snow for each sea-ice category (Bitz and Lipscomb, 1999). Snow is very important for the thermodynamics of sea ice as it insulates sea ice from the atmosphere and has a higher albedo than sea ice. The lower boundary is governed by the upper ocean temperature, which is usually the ocean freezing temperature and is linearly dependent on its salinity. The upper boundary is governed by the heat and radiation transfer between the atmosphere and the combined snow/ice surface. The net heat flux is calculated based on the 2m atmospheric temperature, humidity, incoming long and short-wave radiation, and 10m wind and the state of the surface of the sea-ice model.

The HYCOM and CICE models used in this paper are coupled on each time step using the Earth System modeling Framework (ESMF) coupler (Collins et al., 2004). The HYCOM-CICE set-up at DMI used in this paper covers the Arctic Ocean and the Atlantic Ocean, north of about 20°S, with a horizontal resolution of about 10 km (Madsen et al., 2016)..

70 The HYCOM-CICE model system assimilates re-analyzed sea-surface temperature
 71 (<https://podaac.jpl.nasa.gov/GHRSST>, Høyer et al., 2012, 2014) and sea ice concentration
 72 provided by the EUMETSAT Ocean and Sea Ice Satellite Application Facility (OSI SAF,
 73 www.osi-saf.org, Lavergne et al., 2019) on a daily basis. The model is initialized in summer
 74 1997 using the Polar Science Center Hydrographic Climatology (PHC; Steele et al., 2001) in the
 75 Arctic Ocean and World Ocean Atlas 2001 0.25° (Conkright et al., 2002) in the Atlantic, with a
 76 100 km linear transition. The atmospheric forcing is obtained from the Era-Interim reanalysis
 77 (Dee et al., 2011) until 2017 and thereafter deterministic HRES ECMWF forcing
 78 (www.ecmwf.int).

79 Bitz, C. M. and Lipscomb, W. H.: An energy-conserving thermodynamic model of sea ice, J.
 80 Geophys. Res. Ocean., 104(C7), 15669–15677, doi:10.1029/1999jc900100, 1999.

81 Dai, A. and Trenberth, K. E.: Estimates of freshwater discharge from continents: Latitudinal and
 82 seasonal variations, J. Hydrometeorol., 3(6), 660–687, doi:10.1175/1525-
 83 7541(2002)003<0660:EOFDFO>2.0.CO;2, 2002.

84 Dee, D. P., Uppala, S. M., Simmons, A. J., Berrisford, P., Poli, P., Kobayashi, S., Andrae, U.,
 85 Balmaseda, M. A., Balsamo, G., Bauer, P., Bechtold, P., Beljaars, A. C. M., van de Berg, L.,
 86 Bidlot, J., Bormann, N., Delsol, C., Dragani, R., Fuentes, M., Geer, A. J., Haimberger, L., Healy,
 87 S. B., Hersbach, H., Hólm, E. V., Isaksen, L., Kållberg, P., Köhler, M., Matricardi, M., McNally,
 88 A. P., Monge-Sanz, B. M., Morcrette, J. J., Park, B. K., Peubey, C., de Rosnay, P., Tavolato, C.,
 89 Thépaut, J. N. and Vitart, F.: The ERA-Interim reanalysis: Configuration and performance of the
 90 data assimilation system, Q. J. R. Meteorol. Soc., 137(656), 553–597, doi:10.1002/qj.828, 2011.

91 Egbert, G. D. and Erofeeva, S. Y.: Efficient inverse modeling of barotropic ocean tides, J.
 92 Atmos. Ocean. Technol., 19(2), 183–204, doi:10.1175/1520-
 93 0426(2002)019<0183:EIMOBO>2.0.CO;2, 2002.

94 Hibler, W. D.: A Dynamic Thermodynamic Sea Ice Model, J. Phys. Oceanogr., 9(4),
 95 doi:10.1175/1520-0485(1979)009<0815:adtsim>2.0.co;2, 1979.

96 Høyer, J. L., Karagali, I., Dybkjær, G. and Tonboe, R.: Multi sensor validation and error
 97 characteristics of Arctic satellite sea surface temperature observations, Remote Sens. Environ.,
 98 121, 335–346, doi:10.1016/j.rse.2012.01.013, 2012.

99 Høyer, J. L., Le Borgne, P. and Eastwood, S.: A bias correction method for Arctic satellite sea
 100 surface temperature observations, *Remote Sens. Environ.*, 146, 201–213,
 101 doi:10.1016/j.rse.2013.04.020, 2014.

102 Hunke, E. C.: Viscous-Plastic Sea Ice Dynamics with the EVP Model: Linearization Issues, *J.*
 103 *Comput. Phys.*, 170(1), 18–38, doi:10.1006/jcph.2001.6710, 2001.

104 Large, W. G. and Yeager, S. G.: The global climatology of an interannually varying air - Sea
 105 flux data set, *Clim. Dyn.*, 33(2–3), 341–364, doi:10.1007/s00382-008-0441-3, 2009.

106 Lavergne, T., Macdonald Sørensen, A., Kern, S., Tonboe, R., Notz, D., Aaboe, S., Bell, L.,
 107 Dybkjær, G., Eastwood, S., Gabarro, C., Heygster, G., Anne Killie, M., Brandt Kreiner, M.,
 108 Lavelle, J., Saldo, R., Sandven, S. and Pedersen, L. T.: Version 2 of the EUMETSAT OSI SAF
 109 and ESA CCI sea-ice concentration climate data records, *Cryosphere*, 13(1), doi:10.5194/tc-13-
 110 49-2019, 2019.

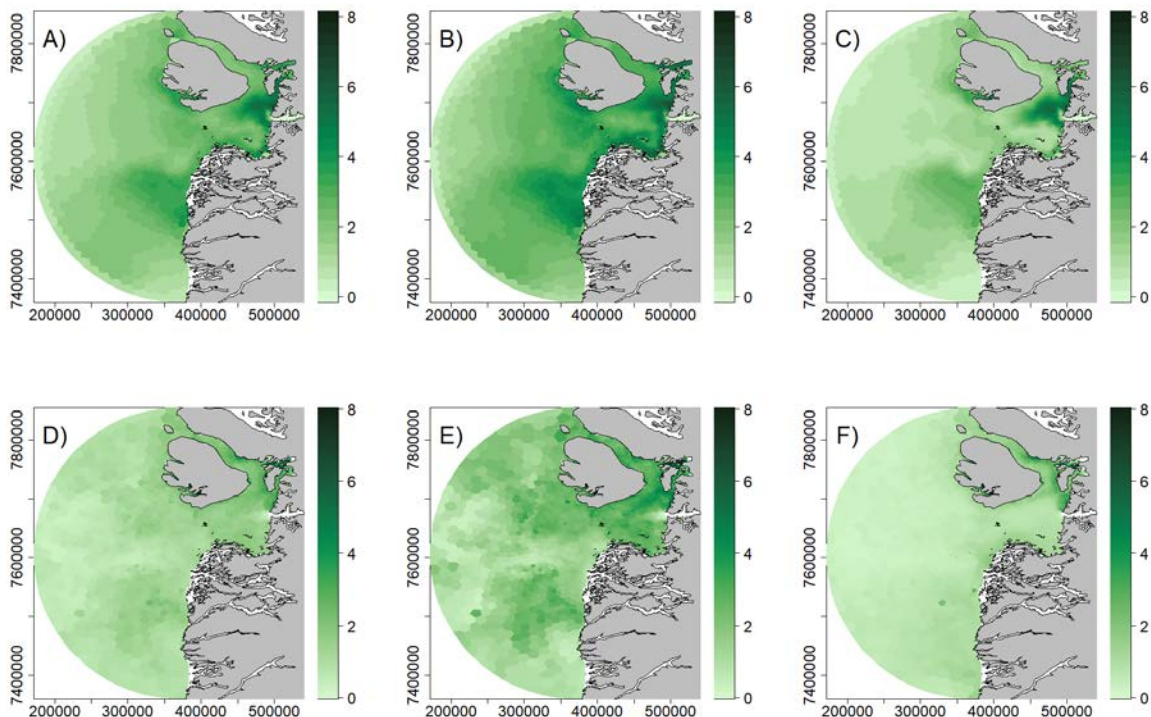
111 Rasmussen, T. A. S., Høyer, J. L., Ghent, D., Bulgin, C. E., Dybkjær, G., Ribergaard, M. H.,
 112 Nielsen-Englyst, P. and Madsen, K. S.: Impact of Assimilation of Sea-Ice Surface Temperatures
 113 on a Coupled Ocean and Sea-Ice Model, *J. Geophys. Res. Ocean.*, 123(4), 2440–2460,
 114 doi:10.1002/2017JC013481, 2018.

115 Steele, M., Morley, R. and Ermold, W.: PHC: A global ocean hydrography with a high-quality
 116 Arctic Ocean, *J. Clim.*, 14(9), 2079–2087, doi:10.1175/1520-
 117 0442(2001)014<2079:PAGOHW>2.0.CO;2, 2001.

118

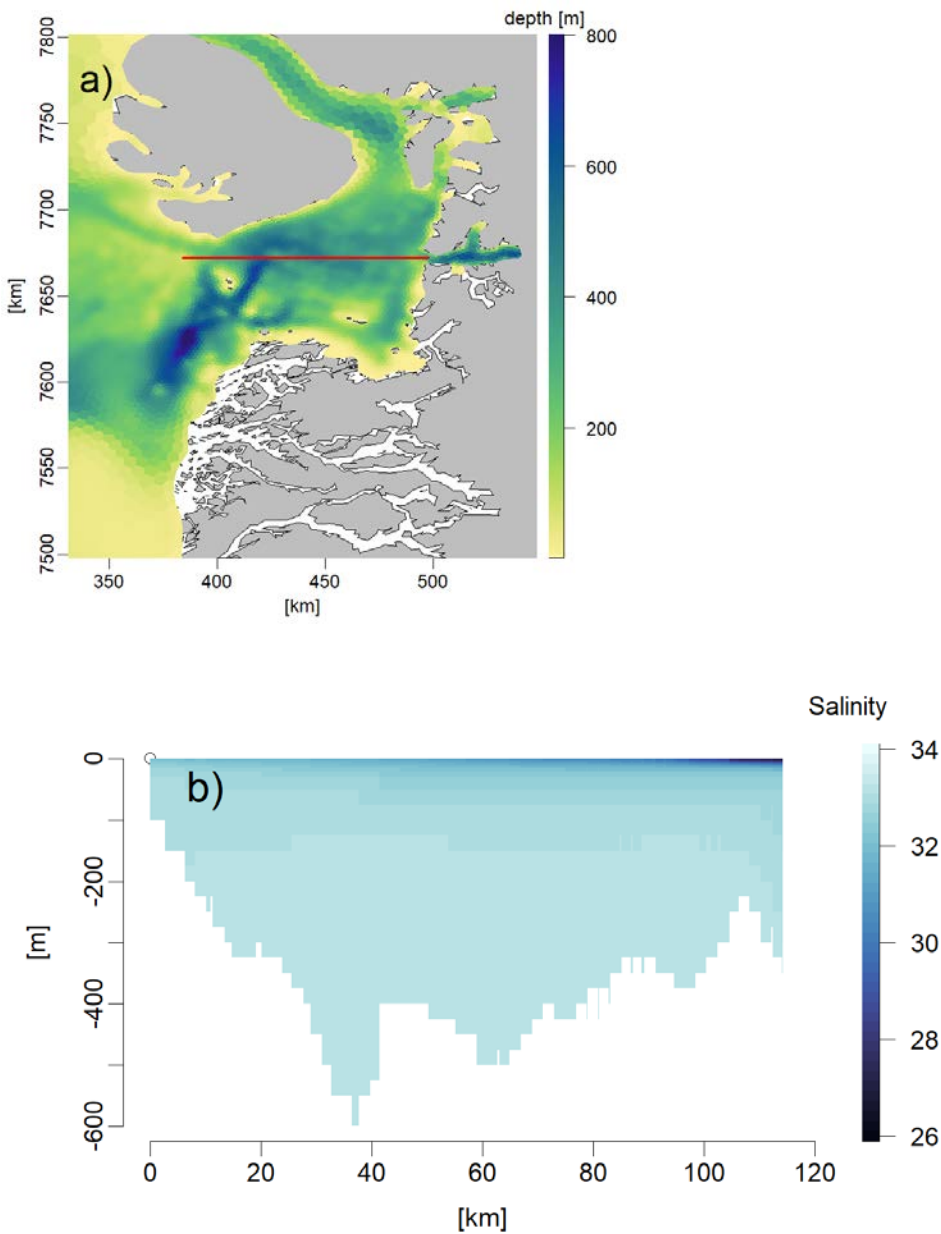
1.3 Supplement, Figures

Figure S1: Surface Chl *a* concentration (mg chl *a* m⁻³) in 2010 obtained from the model (A-C) and from remote sensing (D-F). A) and D) are annual averages, B) and E) are April-June averages, and C) and F) are July-September averages.



122

Figure S2: a) Position and b) bathymetry of transect (x-axis: distance in km, y-axis: depth in m) shown in Figure C3.



123

124

Figure S3: Transects (x-axis: distance in km, y-axis: depth in m) of salinity (a, b) temperature (°C) (c, d), DIN (mmol m⁻³) (e, f), Chl *a* (mg m⁻³) (g, h) and NPP (mgC m⁻³ d⁻¹) (i, j) in April (left) and August (right) 2010 along the transect shown in figure C2:

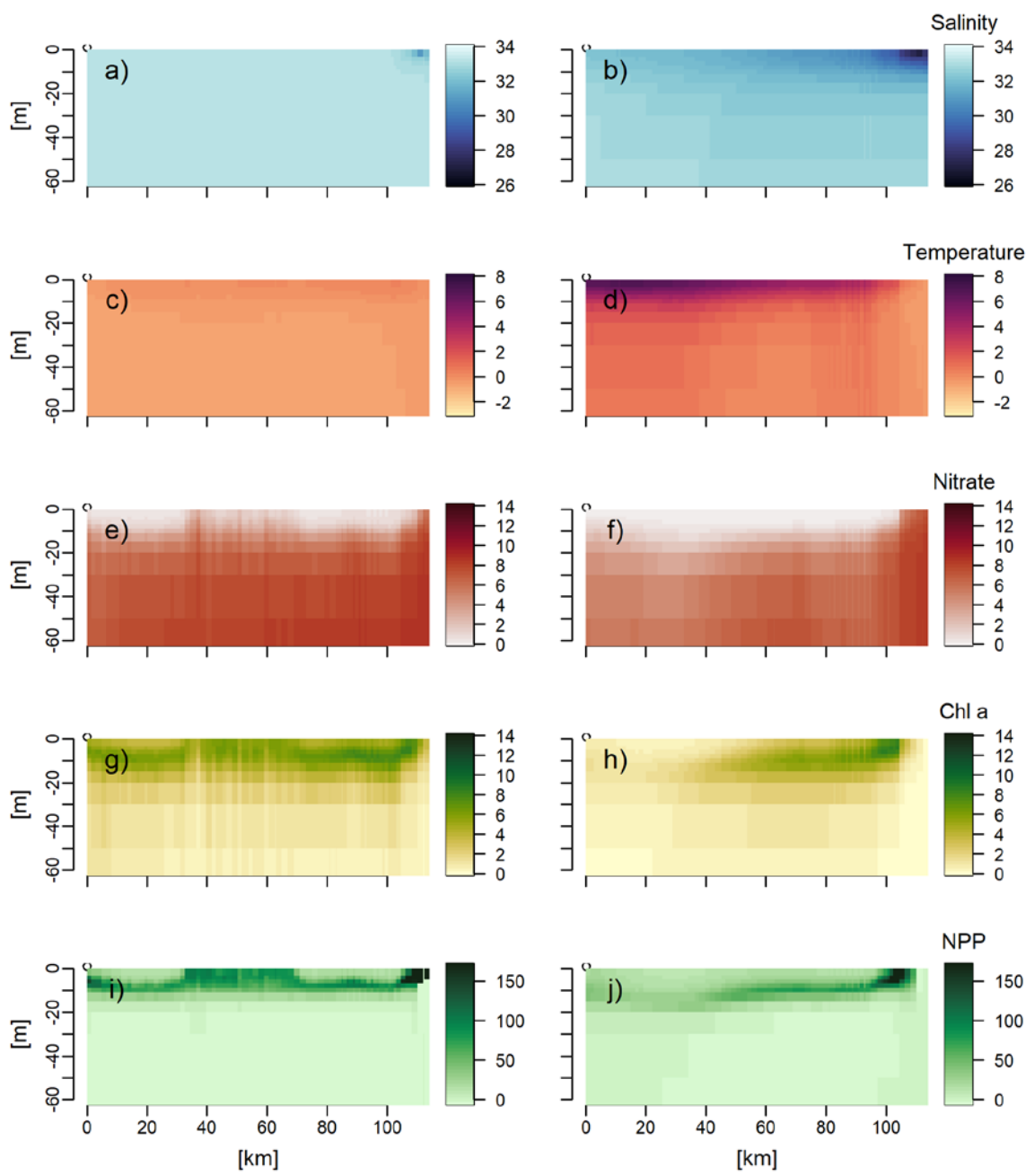


Figure S4. Vertical profiles of a) East-West velocities and b) vertical velocities at the ice edge in Jakobshavn Isbræ for 2010, the scenario noQNP, and the scenario with subglacial discharge at the glacier grounding line.

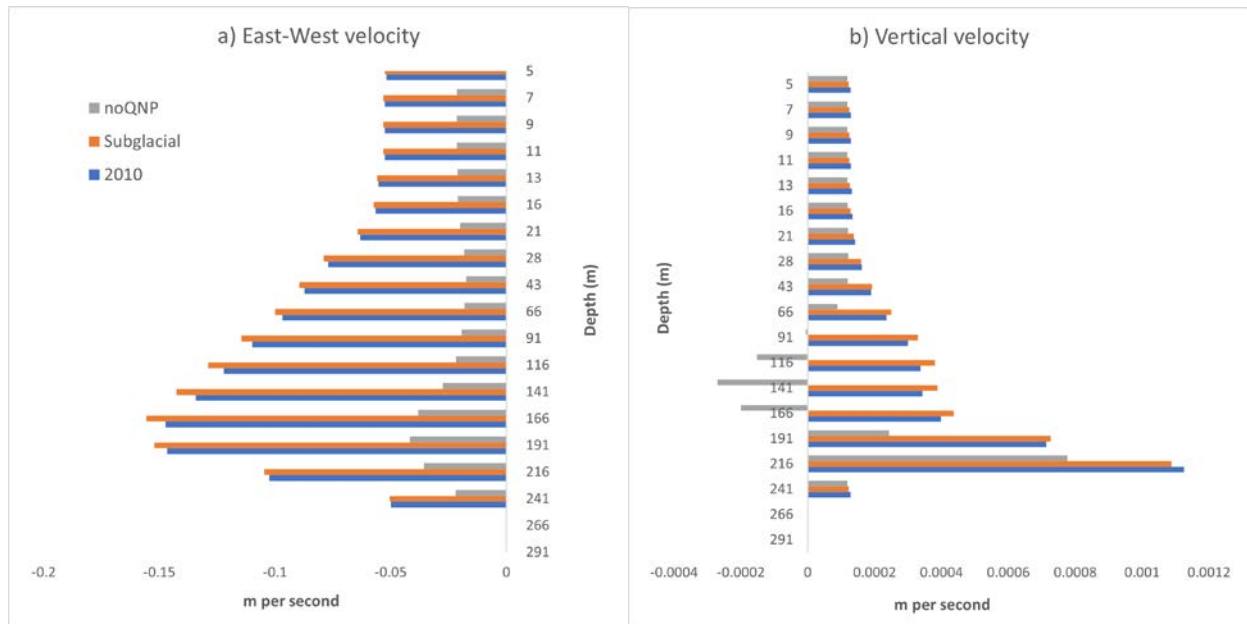
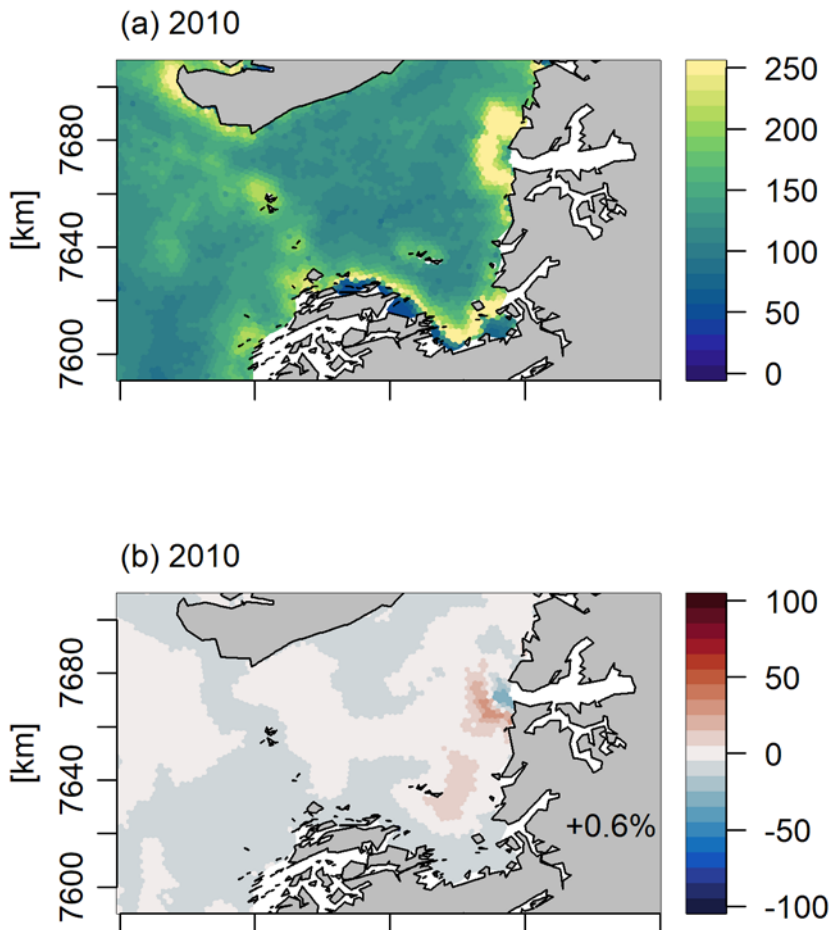


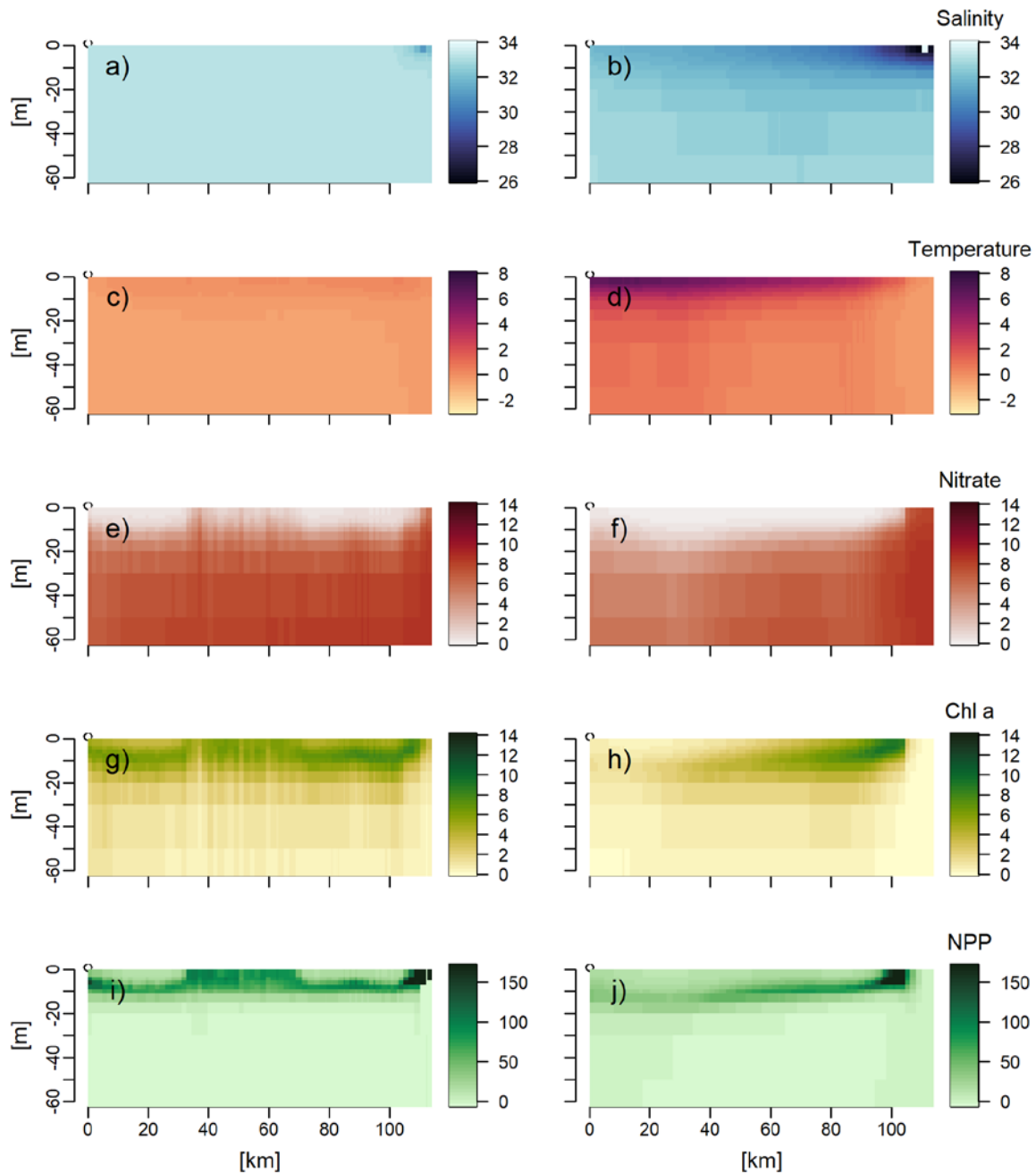
Figure S5: Annual primary production in 2010 (a) when the ice runoff is inserted at the glacier grounding line instead of in the surface as in the standard model run (Fig C3), and percentage change relative to the standard model run (b). The percentages in the bottom of the figure (b) are the changes in primary production in the total area shown.



128

129

FigureS6: Transects (x-axis: distance in km, y-axis: depth in m) of salinity (a, b) temperature ($^{\circ}\text{C}$) (c, d), DIN (mmol m^{-3}) (e, f), Chl *a* (mg m^{-3}) (g, h) and NPP ($\text{mgC m}^{-3} \text{d}^{-1}$) (i, j) in April (left) and August (right) 2010 along the transect shown in figure C2 when the ice runoff is inserted at the glacier grounding line instead of in the surface as in the standard model run (Fig C3).



130

131

